Inorganica Chimica Acta 554 (2023) 121545

Contents lists available at ScienceDirect

Inorganica Chimica Acta

journal homepage: www.elsevier.com/locate/ica

Intermetallic $Au_3Li_xM_{1-x}$ (M = Fe, Ni or Co) nanoalloys: Effect of synthetic conditions on the composition and order-disorder transition

Alessio Gabbani [a,b,*], Elvira Fantechi [a,c], Martin Albino [d,e], Claudio Sangregorio [d,e], Francesco Pineider [a,b,*]

[a] INSTM & Department of Chemistry and Industrial Chemistry, University of Pisa, Via Moruzzi 13, 56124 Pisa, Italy
[b] Department of Physics and Astronomy, University of Florence, Via Sansone 1, 50019 Sesto Fiorentino, Firenze, Italy
[c] Centro di Cristallografia Strutturale, University of Florence, Via della Lastruccia 3, 50019 Sesto Fiorentino, Firenze, Italy
[d] CNR-ICCOM, Via Madonna del Piano 10, 50019 Sesto Fiorentino, Firenze, Italy
[e] INSTM and Department of Chemistry "U. Schiff", University of Florence, via della Lastruccia 3, 50019 Sesto Fiorentino, Firenze, Italy

ARTICLE INFO

Keywords:
Nanoalloys
Intermetallics
Inorganic nanocrystals
Colloidal chemistry
Magnetic-plasmonic nanocrystals

ABSTRACT

Nanoalloys combining magnetic and plasmonic properties are interesting systems for catalysis and photocatalysis, magneto-optics, nanomagnetism and fundamental studies. Nevertheless, their synthesis is challenging due to the immiscibility of Au and 3d magnetic metals at mild temperatures in equilibrium conditions. In this work we prepared through colloidal chemistry synthesis $Au_3Li_xM_{1-x}$ (M = Fe, Ni or Co) nanoalloys and studied the synthetic conditions that affect the transition between a disordered and an ordered $L1_2$ intermetallic alloy crystal phase. We found that Au seeds act as templates for the formation of the intermetallic nanoalloys, and that lithium (coming from the Butyllithium reducing agent injected after the seeds formation) plays a fundamental role in the stabilization of the intermetallic phase. By tuning the synthetic parameters, we were able to tune the Fe content in $Au_3Li_xFe_{1-x}$ intermetallic nanoalloys from 0.6 to 2.6 %, also tuning the magnetic moment of the nanoalloys. All the synthesized nanoalloys were able to sustain a plasmonic resonance in the visible range, which is blue shifted and broadened with respect to Au NPs. Our results can open colloidal synthesis to novel crystal phases and nanomaterials combining plasmonic and magnetic functionalities at the nanoscale.

1. Introduction

Bimetallic inorganic nanocrystals are fascinating nanostructures [1,2] that can merge different properties within a single object, enabling multifarious functionality such as magnetic guiding,[3] exotic magnetic properties,[4] optical and magnetic hyperthermia,[5] peculiar electronic and optical properties,[6] and catalytic activity.[7,8] Such multifunctionality can find application in nanomedicine, catalysis, permanent magnets or sensing.

Among inorganic nanocrystals, metal alloys present unique structural and functional properties which arise from the presence of different metal atoms within the same nano-object.[9] Remarkably, the resulting properties are usually significantly different with respect to bimetallic heterostructures where the two metals form separate domains, such as core@shell or dumbbell nano-heterostructures, resulting in the hybridization of the properties of the single elements involved. In some cases, ordered alloys can be formed, which have different properties than the randomly arranged alloys.[10] It is the case of FePt or CoPt alloys, which upon annealing can form an ordered crystal phase where Pt and Fe (or Co) layers alternate in the unit cells (for this reason ordered alloys are also called intermetallics), also leading to a dramatic increase in the magnetic coercivity with respect to the random alloys, arising from the increased crystalline anisotropy.[11,12] In other cases a significant difference in catalytic activity is observed between intermetallic and random nanoalloys.[13,14] Polar intermetallics made of Au and alkali metals are interesting for the impact of the relativistic bonding interactions on their stabilization,[15–18] with AuLi being the one in which the effect is expected to be more significant,[17] despite it has been poorly investigated with respect to other polar intermetallic compounds made of other alkali metals.[19–22] Therefore, the order–disorder transition represents an important degree of freedom which increases the interest in intermetallic nanoalloys synthesis for both

* Corresponding authors at: INSTM & Department of Chemistry and Industrial Chemistry, University of Pisa, Via Moruzzi 13, 56124 Pisa, Italy.
E-mail addresses: alessio.gabbani@dcci.unipi.it (A. Gabbani), francesco.pineider@unipi.it (F. Pineider).

https://doi.org/10.1016/j.ica.2023.121545
Received 5 January 2023; Received in revised form 31 March 2023; Accepted 26 April 2023
Available online 29 April 2023

fundamental and applied research.

The formation of an alloy is often challenging or requires high temperatures (above 700 °C) due to the low miscibility of the metals involved, such as in the case of the alloys between Au and magnetic metals (Fe, Co or Ni).[23] However, the miscibility of the two metals changes at the nanoscale and a few examples of synthesis of out-of-equilibrium nanoalloys such as AuFe or AuNi have been reported through laser ablation in solution[24,25] or through chemical methods.[26] However, the studies on AuM (M = Fe,Ni,Co) nanoalloys reported in the literature are limited, and the characterization is often incomplete and the synthesis poorly reproducible. The control of the structure and composition of AuM nanoalloys, as well as the elucidation of the mechanism of the alloy formation and order/disorder transition is thus an important task in nanoscience.

The different redox potentials of M and Au introduce additional challenges in the synthesis of the alloy, since the approach of simultaneous co-reduction seems hardly possible in this case, as gold precursors are much easier to reduce with respect to the 3d metal precursors unless a strong reducing agent is used. To this aim, Zhou *et al.*[27] first proposed the use of butyllithium (BuLi) as strong reducing agent to reduce simultaneously Au and Ni precursors, obtaining AuNi alloy NPs for applications in catalysis. Their approach involves the addition of BuLi to a solution of the metal precursors (Au and Ni) and heating up to 250 °C. The authors obtained nanoalloys with atoms of Ni and Au randomly distributed inside the NP, and an average size of about 4.4 nm. Successively, Schaak group[28] reported a slight modification of this approach to prepare Au_3M_{1-x} (M = Fe, Ni, Co) intermetallic alloys with size around 8 nm, and a M content around 18% for Fe, 5–10% for Co and 15–10% for Ni. In a further paper, the same group reported the formation of Au_3Li intermetallic compound through the same synthetic mechanism and proposed its role as intermediate in the formation of the alloy with Ni, Fe or Co.[29] Non-stoichiometry in the Au_3M formula may thus be caused by the insertion of Li atoms in the lattice which are not completely replaced by M atoms. If this is the case, a $Au_3Li_xM_{1-x}$ stoichiometry would be more appropriate for these nanoalloys. However, no evidence of the presence of Li atoms in Au_3M alloys was reported by Schaak group. This may be ascribed to the fact that the analysis of the chemical composition was done through Energy Dispersive X-ray spectroscopy (EDS), a technique which does not allow the detection of Li due to its low atomic number.

In this work, we report a thorough investigation of the synthetic route based on BuLi to obtain $Au_3Li_xM_{1-x}$ (M = Ni, Fe, Co) intermetallic alloys. To this purpose we decided to deliberately introduce lithium in the Au_3M lattice, thus we prepared and studied $Au_3Li_xM_{1-x}$ intermetallic nanoalloys, investigating the effects of several synthetic parameters on the final properties of the nanoalloys. We examined the structural and morphological features of the nanoalloys with a multi-technique approach. The full metal content of the nanoparticles (NPs) was determined by Inductively Coupled Plasma Atomic Emission Spectroscopy (ICP-AES), a technique which is also sensitive to lithium. We found that the intermetallic phase is composed mostly of lithium (20–25 %) with a minor amount of M metals (below 1%), despite a precursor stoichiometry of Au_3M. By investigating the effect of synthetic parameters on the crystal structure of the final product, determined through X-ray Powder Diffraction (XRPD), we identified the conditions that allows obtaining selectively the random alloy or the intermetallic phase. Moreover, we confirmed that the reaction mechanism that yields the intermetallics involves first the formation of Au seeds by reduction with oleylamine. The seeds act as templates for the formation of the nanoalloys after the injection of BuLi. We also investigated the stability of the intermetallic nanoalloys with heating time at 250 °C, revealing that loss of M metals from the NPs occurs after prolonged heating. A plasmonic resonance was observed for the synthesized intermetallic alloys, blue shifted and broadened with respect to Au NPs. The amount of Fe atoms in the nanoalloys was found to increase up to 2.6% by increasing the temperature of the final step of the reaction to the boiling point of the reaction mixture (265 °C), resulting also in an increase in the magnetic moment of the nanoalloys.

2. Results and discussion

The synthetic procedure employed was adapted from the method developed by Bondi et *al.*.[28] Briefly, $M(acac)_x$ (M = Ni, Fe or Co) and Au precursor ($HAuCl_4$) were dissolved in diphenyl ether (DPE) in the presence of oleylamine (OLAM) and heated to an initial temperature T_i after which an excess of BuLi was quicky injected to this solution and the temperature was raised to a dwell temperature T_f (initially set to 250 °C) over 80 min. After the temperature reached T_f, the heating source was removed, and the mixture was cooled down to room temperature. All the synthetic steps were carried out in air-free conditions, under Ar atmosphere. The detailed synthetic protocol is reported in Methods.

The obtained nanoalloys were characterized with a multi-technique approach: X-ray powder diffraction (XRPD) was used to confirm the presence of the alloy and determine whether it is an intermetallic or a random alloy, Transmission Electron Microscopy (TEM) to study the size and the morphology of the NPs, and ICP-AES to determine the atomic composition.

The heating program is crucial for the formation of the alloy, and to control the formation of random or intermetallic phases. The effect of heating time and temperature in the first step of the synthesis was investigated for the $Au_3Li_xNi_{1-x}$ system, as well as the stability of the intermetallic phase by increasing the time of the final step of the reaction at 250 °C. Finally, the last step of the temperature protocol was modified for the $Au_3Li_xFe_{1-x}$ system, aiming at increasing the Fe content in the nanoalloys, as well as their magnetic moment. The general scheme of the synthesis is depicted in Fig. 1, in which the conditions that yield the random and intermetallic alloys are indicated with a green or blue line respectively.

Effect of the injection temperature of BuLi. The first step of the reaction involves the dissolution of the precursors and the heating of the reaction mixture before the injection of BuLi, which is crucial to control the final size of the NPs. In particular, the temperature of the reaction mixture before BuLi addition is an important parameter to control both size, polydispersity and crystal phase of the nanoalloys.

According to the nucleation and growth theory,[30] the stronger is the reducing agent, the faster is the reduction process and the smaller are the initial seeds formed, which then grow forming the final NPs during the following step. In the reaction mixture, two reducing agents are present: OLAM, which is known to be a good reducing agent to form Au NPs in organic solvents[31,32] even at mild temperatures and BuLi, much stronger than OLAM, necessary to reduce M (M = Fe, Co, Ni) ions, which are characterized by large and negative redox potentials. In first instance, the use of such a strong reducing agent is expected to produce smaller NPs due to the co-reduction of both metal precursors. However, we must take into account that, depending on the reaction conditions, the presence of OLAM could lead to the formation of Au NPs before the injection of BuLi, thus strongly influencing the dynamics of the nucleation and growth. In this framework, the heating temperature of the initial stage is crucial to form Au NPs before BuLi injection. In fact, by heating the Au and M precursors at 60 °C, no formation of NPs was observed, but when the temperature was raised to 70–80 °C the reaction mixture became dark red, indicating the presence of Au NPs.

Therefore, when the BuLi solution was injected at 60 °C, a fast reduction of $HAuCl_4$ and $Ni(acac)_2$ occurred, leading to NPs of around 4 nm (Fig. 1). At 60 °C the reduction of $HAuCl_4$ has not started, and simultaneous reduction of the two metals is likely to occur upon the addition of BuLi. In this case, superlattice peaks typical of an ordered intermetallic phase are not observed in the XRPD diffraction pattern (Fig. 2 c), indicating a random arrangement of the metals in the alloy. This is consistent with the work by Zhou *et al.*,[27] where BuLi was injected at low temperature (40–50 °C) and random AuNi alloys were obtained.

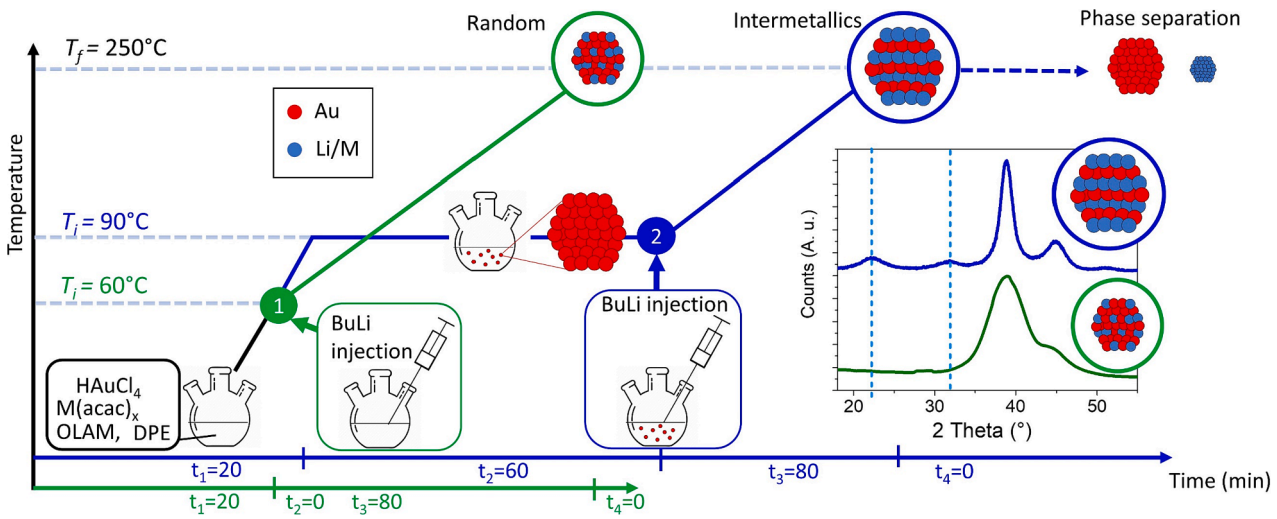

Fig. 1. Scheme of the synthetic route for obtaining the random $Au_3Li_xM_{(1-x)}$ nanoalloy (indicated with a green line), and the optimized temperature program for the intermetallic $Au_3Li_xM_{(1-x)}$ nanoalloy (indicated with a blue line). The inset highlights the differences in the XRPD pattern of the two synthesized nanoalloys, where the superlattice peaks of the $L1_2$ intermetallic phase are highlighted by the vertical dashed pale-blue lines. The heating times of each synthetic step is indicated in the bottom axis in green for the random and in blue for the intermetallic alloy synthesis. In the first case BuLi is injected when the precursors are still unreacted (60 °C), while for the latter case the BuLi is injected after the Au seeds are formed by in situ reduction with OLAM for 1 h at 90 °C.

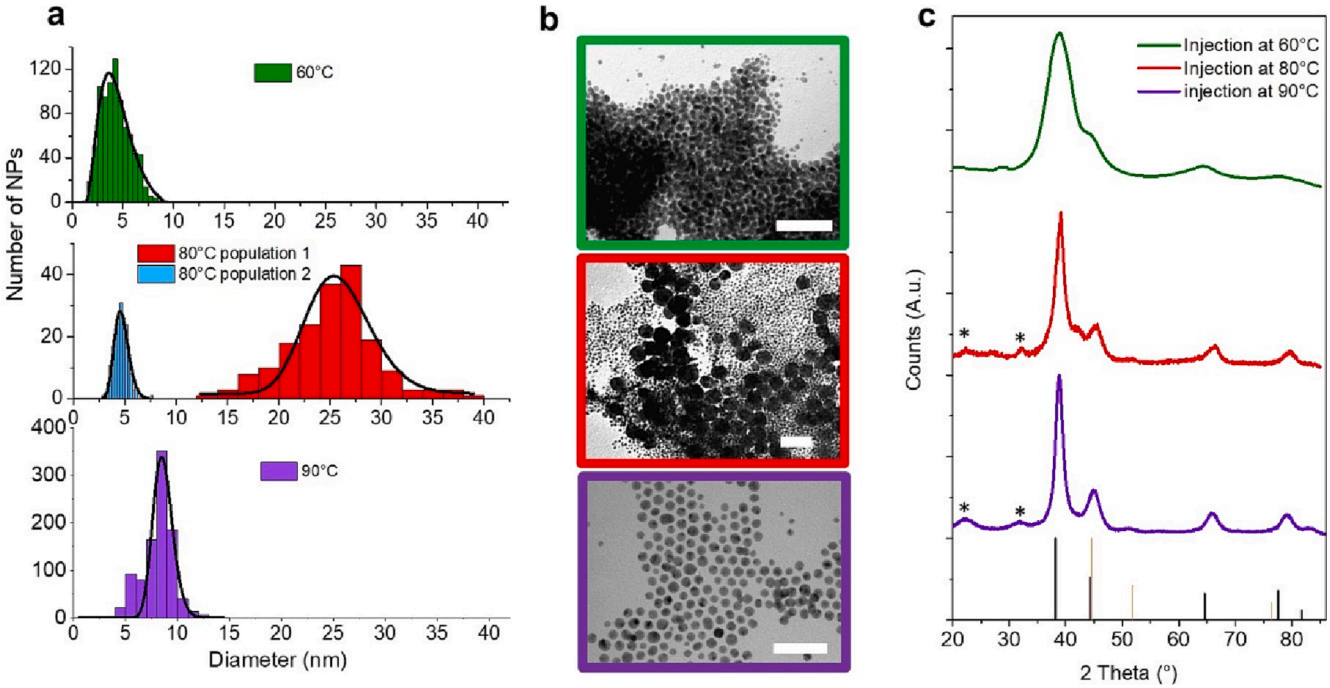

Fig. 2. Size distributions (A), TEM images (B), and X-ray Diffraction pattern (C) of Au_3Ni nanoalloys prepared by injecting BuLi at 60 °C, 80 °C and 90 °C. Scale bar in TEM images is 50 nm. Au and Ni reference patterns are shown as vertical black and orange lines, respectively. The superlattice peaks typical of the $L1_2$ intermetallic phase are marked with an asterisk in (C). A Cu k_α X-ray source was used for XRPD analysis.

On the other hand, when the injection of BuLi was performed after heating the reaction mixture at 80 °C for 30 min, two size populations of NPs were obtained, as reported in Fig. 2 a, b. The superlattice peaks typical of the $L1_2$ intermetallic alloy are now visible in the XRPD pattern (Fig. 2 c). The temperature and time at which the precursors were heated before BuLi addition is thus a crucial parameter to obtain random alloys or intermetallic NPs: by short heating time at low temperature (60 °C) random alloys are obtained, while heating for longer time at higher temperature (30 min at 80 °C) induces the growth of the intermetallic phase.

The formation of two populations of NPs is probably related to the presence of two successive nucleation events: (i) the first at 80 °C with OLAM as mild reductant, a slow process that gives rise to larger Au NPs (~25 nm); (ii) the second after the addition of BuLi, a fast nucleation of the unreacted precursors which results in the formation of smaller NPs (~5 nm).

Such a double population of NPs suggests that not all the Au precursor was reduced by OLAM in the first step. In order to make sure that all the $HAuCl_4$ is consumed in the first step of the synthesis, the amount of OLAM was increased to 0.5 mL and the temperature T_1 was raised to 90 °C. An aliquot of the reaction mixture was taken every 10 min and the particles were separated from the reaction mixture by centrifugation in

ethanol. By keeping the ethanol supernatant solution overnight, if Au precursor is still present in solution, it will react slowly with OLAM leading to the formation of a dark precipitate, which consists of large and aggregated Au NPs due to the destabilizing action of ethanol. Fig. S1 shows pictures of the supernatant solutions of different aliquots taken at different reaction times, a day after the synthesis. In the aliquots taken before 40 min, a dark precipitate was formed at the bottom of the vials, indicating that unreacted Au precursors were still present in the reaction mixture when the aliquot was taken. The dark precipitate disappeared only in the aliquots taken after 40 min at 90 °C, resulting in clear yellow solutions. Based on these findings, we modified the synthetic route as follows: the reaction mixture was heated at 90 °C for 1 h with 1 mL of OLAM in the first step of the reaction, to ensure that all Au precursor reacted before the addition of BuLi, avoiding the secondary nucleation. *In situ* formation of Au seeds, with size around 12 nm, and a diffraction pattern consistent with that of pure Au (Fig. S2) was obtained in this first step. With these modifications, it was possible to obtain a single population of NPs with size around 8.5 nm, and with an intermetallic crystal structure (inset in Fig. 1). All the successive syntheses were performed with these adjustments in the first step of the synthetic protocol.

In summary, direct BuLi injection at 60 °C gives rise to random nanoalloys with size around 4 nm, while heating for 1 h at 90 °C the reaction mixture before BuLi addition leads to intermetallic NPs with a diameter around 8.5 nm (Fig. 1). Injection temperature is thus a key parameter to control the size and the crystal phase of the synthesized nanoalloys. Our findings suggest that a critical size needs to be exceeded to obtain the ordered intermetallic phase, while small nanoalloys tend to keep the random configuration. This is consistent with a size-dependent driving force for the disorder–order transition in nanoalloys.[33] Such size-dependence is affected both by thermodynamic and kinetic parameters.[14] From a thermodynamic point of view, the change in free energy is usually negative going from a disordered to an ordered phase, thus representing the driving force for the formation of an ordered alloy. [14] However, the total surface free energy of NPs increases with decreasing size, thus reducing the driving force for the formation of the ordered phase. From the kinetic point of view, phase transitions are facilitated if atom diffusion is faster, and the barrier for atom diffusion is smaller for NPs with respect to the bulk. In summary, smaller NPs enable faster atom transport but restrict the formation of a new phase, which suggests there is an optimal size in which the intermetallic phase is achieved at a given temperature, as also reported for different alloys. [34]

Optimized synthetic protocol: chemical and structural characterization. On the basis of the results of the investigation reported in the previous section an optimized synthetic protocol (indicated in blue in Fig. 1) was designed to obtain selectively the intermetallic $Au_3Li_xNi_{1-x}$ nanoalloy, rather than the random one.

The synthesis of the intermetallic nanoalloy was then extended to other magnetic metals, namely Fe and Co, and a control synthesis was performed with the same protocol but without $M(acac)_x$ (in the following labelled as Au_3Li-0). In the control synthesis the formation of Au seeds was faster and BuLi was added after 40 min at 90 °C (instead of 1 h). Elemental analysis (ICP-AES) highlighted an Au_3Li stochiometric nanoalloy. The XRPD patterns (Fig. 3) of all the samples show the superlattice peaks typical of the $L1_2$ intermetallic phase, even in the absence of $M(acac)_x$. This suggests the initial formation of an intermetallic compound between Au and Li, followed by the incorporation of M (Ni, Fe or Co) in the crystal lattice. ICP-AES analysis indicated that only a small amount of M was incorporated in the NPs, while a significant amount of Li atoms (around 20–25%) was present (Table 1).

Size distributions of the samples are reported in Fig. 4, together with the mean diameter and its standard deviation. Au_3Li-0 is more polydisperse than the $Au_3Li_xM_{(1-x)}$-0 NPs synthesized in the presence of $M(acac)_x$. This suggests a possible role of the metal acetylacetonate in the size control of the NPs. Furthermore, the polydispersity strongly increases in the second step of the reaction, after the addition of BuLi (see

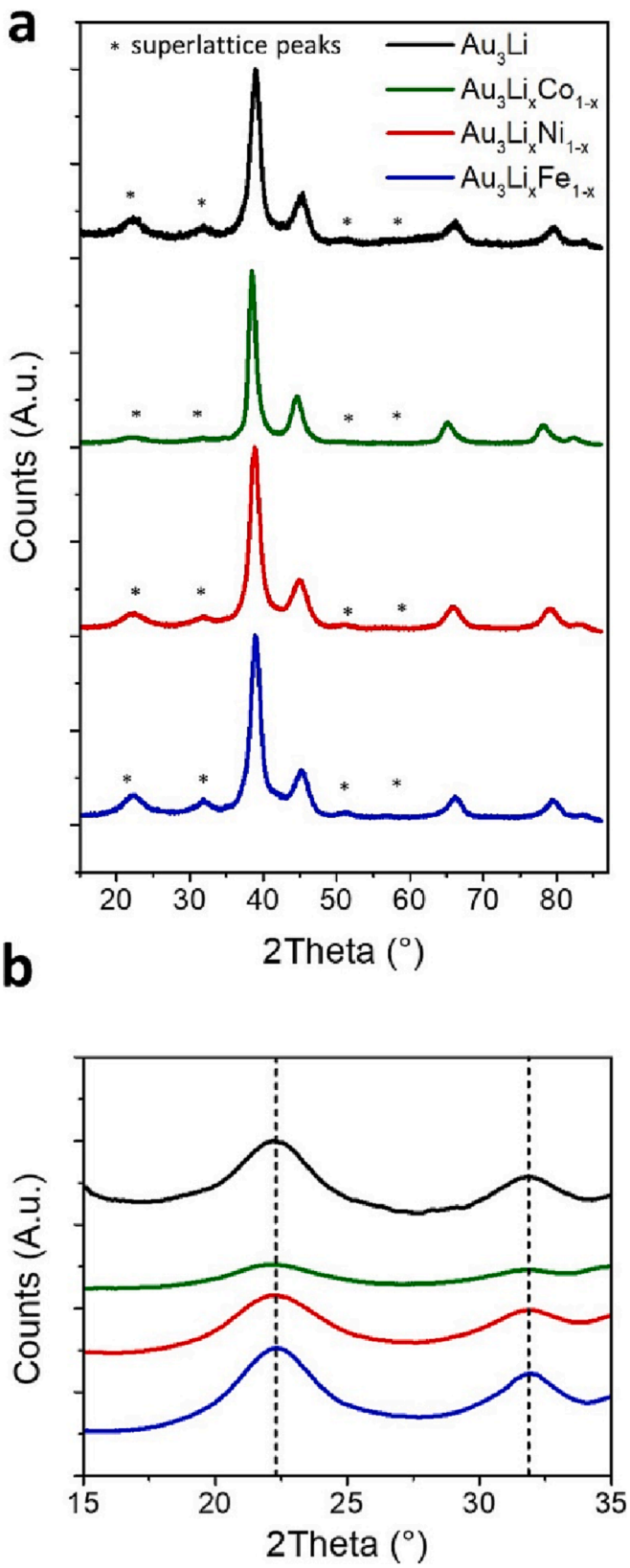

Fig. 3. X-ray Powder Diffraction pattern of the synthesized intermetallic nanoalloys (a), where the superlattice peaks typical of the intermetallic phase are marked with an asterisk. Panel (b) highlights the region of the superlattice peaks. A Cu k_α X-ray source was used.

Table 1
Elemental composition determined by ICP-AES for the $Au_3Li_xM_{(1-x)}$ nanoalloys.

Sample	Atomic % (ICP-AES) Au	M	Li
Au_3Li-0	70.04	0	29.96
$Au_3Li_xFe_{(1-x)}$-0	78.89	0.56	20.55
$Au_3Li_xCo_{(1-x)}$-0	79.67	0.17	20.16
$Au_3Li_xNi_{(1-x)}$-0	78.74	1.74	19.52

size distributions in Fig. 4 d).

On the basis of XRPD and TEM investigations, the presence of (Table 2) a separate Li rich phase in the sample can be excluded. We can thus conclude that the synthesized nanoalloys are trimetallic $Au_3Li_xM_{(1-x)}$ alloys.

Optical properties. Metallic NPs typically exhibit a localized surface plasmon resonance (LSPR), whose spectral position may range from the UV–vis (noble metals[35]) to the infrared (heavily doped semiconductors[36]) depending on the type of material. LSPR can be exploited for photo-catalysis,[37] heat generation,[38–40] or sensing.[41,42] The LSPR peaks of $Au_3Li_xM_{(1-x)}$ and Au_3Li (Fig. 5) are broadened and blue shifted with respect to the Au seeds, as already found in previous investigations for AuFe alloy NPs.[24,25] This can be explained with a modification of the dielectric function of the alloy with respect to Au: the introduction of 3d metals (Fe, Ni or Co) results in higher optical losses due to interband transitions that damp the plasmonic resonances. Such a blue shift of the plasmonic resonance is a clear fingerprint of the formation of an alloy, ruling out the formation of heterostructures or a thin metal oxide shell at the surface of the nanoalloys. Indeed, in a core@shell structure one would expect a surface oxidation of the magnetic metal shell upon air exposure to form $Au@MO_x$ NPs, leading to a red shift of the plasmonic resonance, as previously observed in $Au@FeO_x$ NPs.[5,43] On the other hand, the formation of the alloy seems to protect magnetic metal ions from oxidation, as suggested by the blue shift and broadening of the LSPR peak. Indeed, the onset of interband transitions can change upon alloy formation with respect to the bare metals. A similar effect is probably caused by the presence of lithium, as it is observed also in Au_3Li. Experimental observation of plasmonic properties in such intermetallic alloy has not been reported in the literature. However, *ab initio* calculations have revealed a modification of the band structure for AuLi, with the onset of the interband transition red shifting to lower energy (0.3 eV compared to 2.25 eV of Au),[44] suggesting an overlap with the plasmonic resonance that can be responsible of the plasmon broadening.

A reduced broadening and blue shift of the plasmonic peak is observed for the $Au_3Li_xCo_{1-x}$ nanoalloy, coherently with the lower amount of magnetic metal (Co, 0.17%). The addition of an excess of OLAM enhances the stability of the dispersion, avoiding aggregation, that usually causes a broadening and red shift of LSPR peaks (Fig. 5 b.)[45] This treatment was used to collect all the spectra of the nanoalloys.

Stability of the intermetallic phase with time at 250 °C. The stability of the intermetallic phase was investigated for the $Au_3Ni_xLi_{(1-x)}$ alloy by tuning the final heating time (t_4) at 250 °C from 0 to 60 min. The intermetallic crystal phase is still present if the reaction mixture is kept at 250 °C for 40 min. After 50 min at 250 °C, the superlattice peaks disappear, and the diffraction peaks of the NPs shift to lower 2θ (see the inset in Fig. 6 a), with a decrease of the lattice constant which becomes close to that of pure Au. This is consistent with a lower Ni content of the alloy, or with a phase segregation of the two metals (Au and Ni). In particular, the metal content obtained through ICP-AES suggests that the Ni content decreases with the increase of heating time up to 40 min – thus suggesting that the intermetallics incorporates less Ni - while it increases again after 1 h, suggesting a segregated Ni phase.

The UV–vis spectra (Fig. 6 b) show the increase in intensity and decrease in peak width as well as a red shift of the plasmonic absorption, which looks closer to the one of pure Au NPs, confirming the hypothesis of phase separation between Au and Ni.

Effect of the increase of the dwell temperature on the Fe content. With the aim to increase the amount of Fe incorporated in the

Table 2
Reaction conditions and metal composition for the $Au_3Li_xNi_{1-x}$ alloys.

	[a] t_3 (min)	[a] T_f (°C)	[a] t_4 (min)	Au % (ICP)	Ni % (ICP)	Li % (ICP)
$Au_3Li_xNi_{1-x}$-0	80	250 °C	0	78.74	1.74	19.72
$Au_3Li_xNi_{1-x}$-20	80	250 °C	20	79.15	0.93	19.92
$Au_3Li_xNi_{1-x}$-40	80	250 °C	40	86.45	0.25	13.3
$Au_3Li_xNi_{1-x}$-50	80	250 °C	50	N.A.	N.A.	N.A.
$Au_3Li_xNi_{1-x}$-60	80	250 °C	60	87.61	2.94	9.45

a) reaction parameters are defined according to the temperature program shown in Fig. 1.

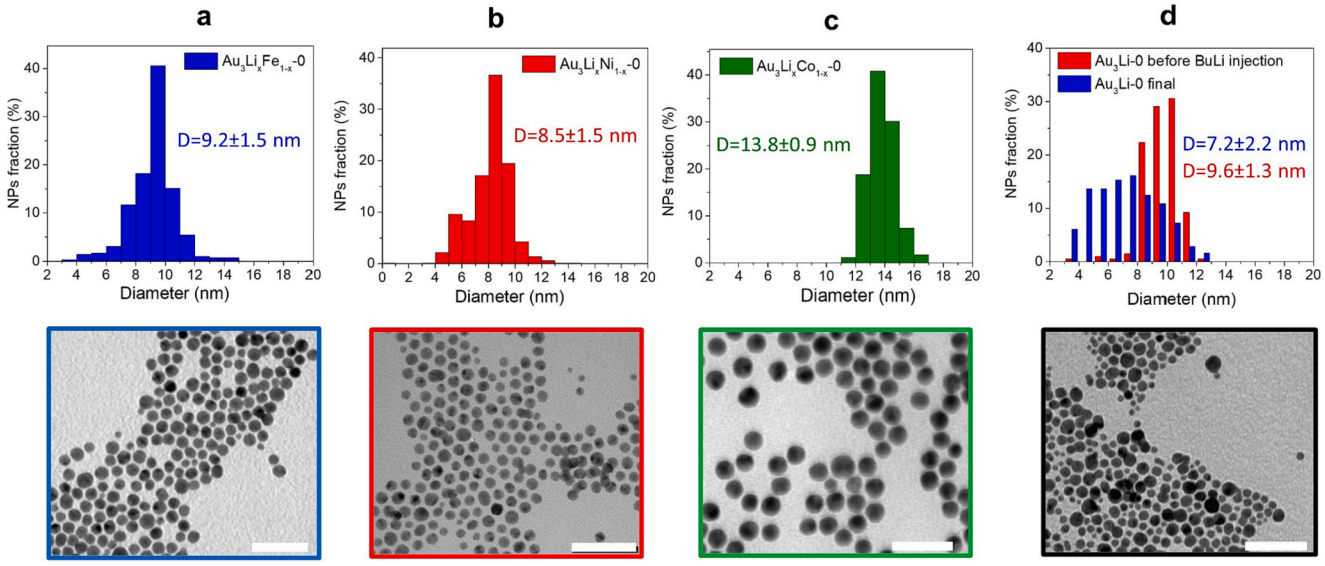

Fig. 4. Representative TEM images (bottom panel) and size distributions (top panel) of $Au_3Li_xFe_{1-x}$-0, $Au_3Li_xNi_{1-x}$-0, $Au_3Li_xCo_{1-x}$-0 and Au_3Li-0. Average diameter (D) ± standard deviation is reported on the graph. In the case of Au_3Li, also the size distribution of Au seeds formed *in-situ* before BuLi injection is reported. Scale bar in TEM images is 50 nm.

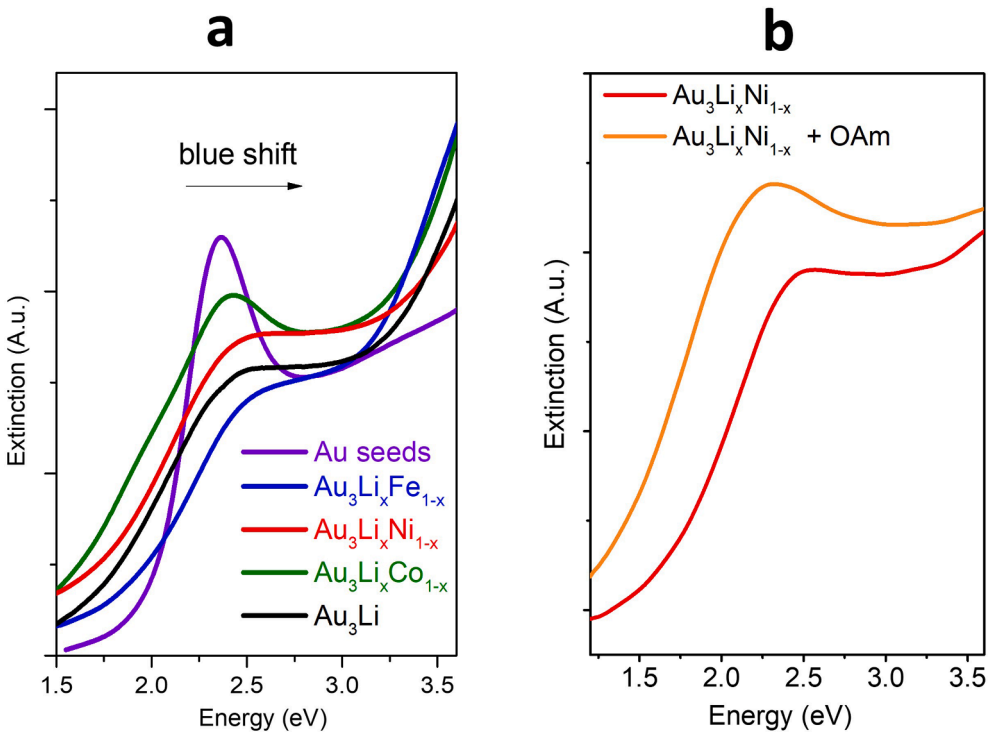

Fig. 5. UV–vis spectra (a) of the synthesized $Au_3Li_xM_{(1-x)}$ nanoalloys dispersed in toluene and effect of the addition of an excess of OLAM on the plasmonic properties (b).

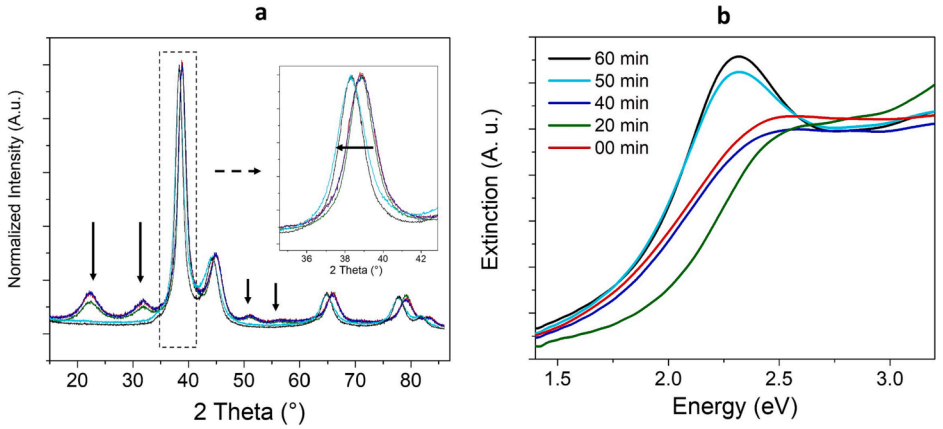

Fig. 6. XRPD (a) and UV–vis spectroscopy (b) characterization of $Au_3Li_xNi_{(1-x)}$ nanoalloys kept at 250 °C for a different time. The inset in the (a) highlights the change of the position of the most intense diffraction peak.

intermetallic NPs, the final temperature T_f was modified in the heating program, according to Table 3. ICP analysis revealed that increasing T_f from 250 °C to the boiling temperature of the reaction mixture (264 °C), the amount of Fe in the intermetallic alloy increases from 0.6 to 2.6 %, while maintaining the intermetallic crystal structure, as confirmed by the presence of the superlattice peaks in the diffraction pattern (Fig. 7 a). Nevertheless, a considerable amount of lithium is still present in the nanoalloys. Plasmonic properties are maintained, with a broadening and blue shift with respect to pure Au NPs, similarly to the previous samples (Fig. 7 c). No significant changes in the morphology and size of the NPs are observed in these samples (TEM images of some of the samples are reported in Fig. 7 b).

A further increase in the final temperature T_f was achieved by changing the solvent from diphenyl ether to octyl ether, which has a boiling temperature of 292 °C, but no increase in the amount of Fe incorporated in the nanoalloys was observed.

The use of a lithium-free reducing agent such as tetrabutylammonium borohydride (leaving all the other reaction parameters unchanged) resulted in the formation of pure Au NPs of larger size, without incorporation of Fe, as confirmed by the XRPD pattern which is comparable to the reference pattern of Au (Fig. S3). These findings confirm the crucial role of lithium incorporation in the formation of the intermetallic alloy.

Magnetic and magneto-optical properties. The magnetic properties of some of the $Au_3Li_xFe_{(1-x)}$ nanoalloys were studied through SQUID magnetometry (Fig. 8). The magnetization detected at 5 Tesla is relatively low, even at 2.5 K, due to the low Fe content of the alloy, and it increases nearly linearly with the iron content (Table 3).

The Magnetic Circular Dichroism (MCD) spectrum of $Au_3Li_xFe_{1-x}$-264 °C dispersed in toluene was collected at 1.4 Tesla at room temperature and is reported in Fig. 9, together with the extinction spectrum of the same solution. Magnetic modulation of the plasmonic resonance has

Table 3
Modification of the temperature program, final metal composition determined through IPC-AES and magnetization at 5 Tesla and 2.5 K detected through SQUID magnetometry.

	[a] $t_{3\ (min)}$	[a] $T_{f\ (°C)}$	[a] $t_{4\ (min)}$	Au %	Fe %	Li %	M_{5T} @ 2.5 K (emu/g)
$Au_3Li_xFe_{1-x}$ −0	80	250	0	78.72	0.57	20.71	0.10
$Au_3Li_xFe_{1-x}$-264 °C	80	264	0	74.93	1.28	23.79	0.15
$Au_3Li_xFe_{1-x}$-264 °C-30 min	80	264	30	74.88	2.66	22.45	0.32
$Au_3Li_xFe_{1-x}$-292 °C	80	292	0	80.19	0.52	19.29	N.A.

a) reaction parameters are defined according to the temperature program shown in Fig. 1.

been demonstrated in different systems, including nonmagnetic plasmonic NPs (such as noble metal[46,47] and transparent conductive oxide[48]), magnetic nanostructures such as ferromagnetic Ni nanodisks,[49] and more complex architectures prepared by lithographic techniques such as metal-dielectric hyperbolic NPs and non-concentric ring-dot nanostructures.[50–52] In the simplest case of noble metal NPs, such effects arise fundamentally from the magnetic field driven Lorentz force experienced by conduction electrons, which in MCD results in a derivative-like signal centred at the LSPR.[46] Also in our nanoalloys a MCD signal ascribed to the LSPR is observed, with the typical derivative-like shape, crossing the zero at the LSPR maximum. At higher energy, a negative MCD contribution appears, which can be ascribed to the interband transitions of the alloy, modified for the presence of Li and Fe. The magneto-optical response at the plasmon resonance energy is consistent with a model based on magnetic field induced energy shift of circular magnetoplasmonic modes.[46] Scanning the magnetic field at different photon energies reveals a linear field-dependence of the MCD signal, typically observed in noble metal NPs up to very high fields,[53] thus ruling out the presence of a magnetic coupling between Au and Fe (consistently with magnetometric data), which has been observed on different bimetallic plasmonic-magnetic hetero-nanostructures.[54–57].

3. Conclusions

In this work we study the formation of $Au_3Li_xM_{1-x}$ (M = Ni, Fe, Co) intermetallic nanoalloys, confirming the critical role played by lithium in stabilizing the intermetallics. By tuning the synthetic parameters, it is possible to synthesize random alloy, or the intermetallic phase. In the case of the random alloy, 4 nm NPs are formed by co-reduction with BuLi, while for the intermetallic phase larger NPs are formed (8–9 nm). We also investigated the stability of the intermetallic phase with the heating time at 250 °C, demonstrating that the intermetallics is stable up to 40 min, while at longer heating time the intermetallic peaks disappear, leading to a diffraction pattern consistent with Au NPs. Moreover, we demonstrate the possibility to increase the amount of iron loaded in the alloy (from 0.6 % to 2.6 %) by increasing the final heating temperature to 264 °C. The presence of lithium in the alloy is ubiquitous in all the investigated systems, as demonstrated by the control synthesis performed without the 3d magnetic metals. Our findings suggest that

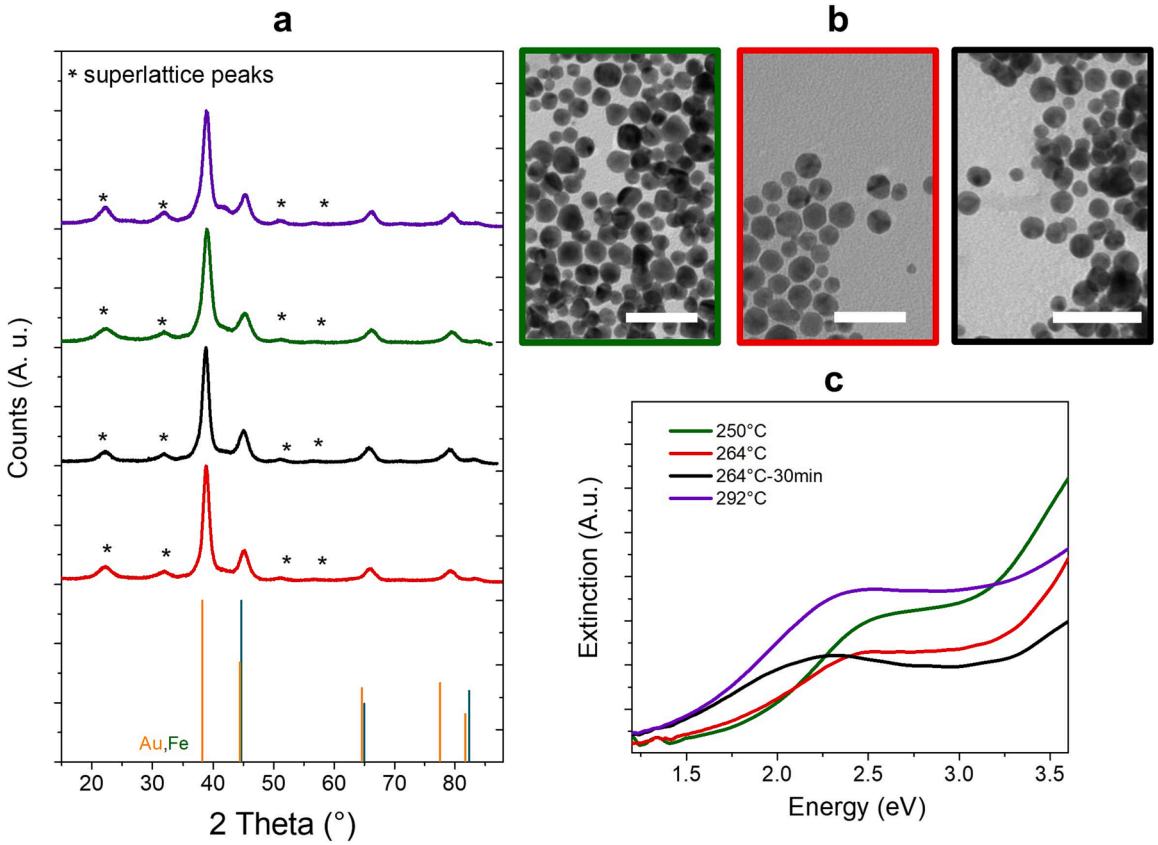

Fig. 7. X-ray diffraction pattern (a) of the $Au_3Li_xFe_{1-x}$ samples, representative TEM images (b) for three samples (scale bar is 50 nm), and corresponding UV–vis spectra (c).

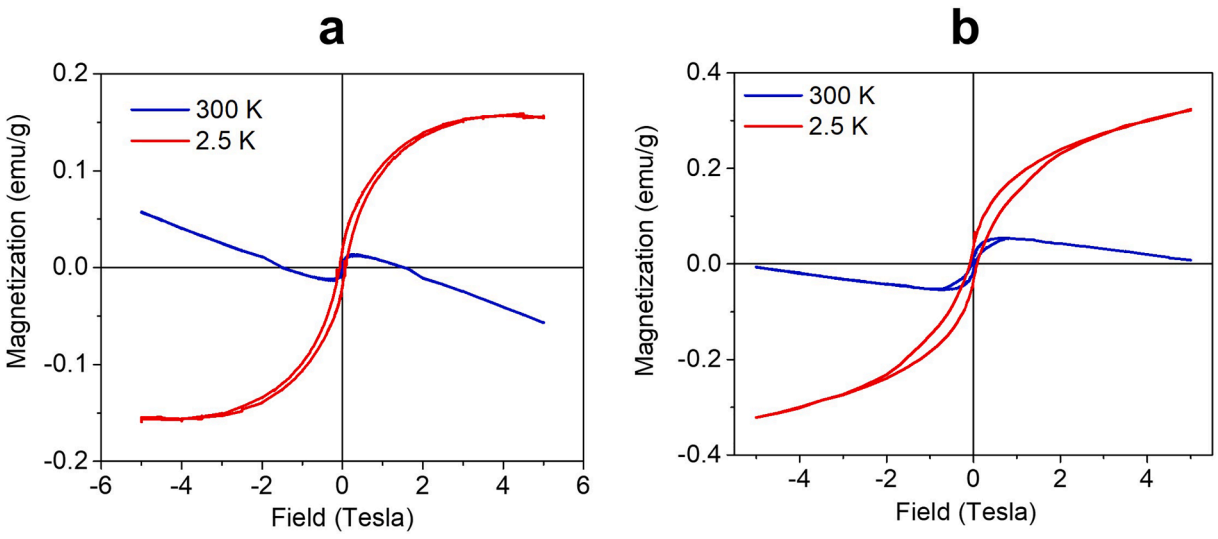

Fig. 8. Hysteresis loops for $Au_3Li_xFe_{1-x}$-264 °C (a) and for $Au_3Li_xFe_{1-x}$-264 °C-30 min (b), collected with a SQUID magnetometer. The magnetization is normalized for the total mass of sample, and the diamagnetic contribution of the Teflon support was subtracted.

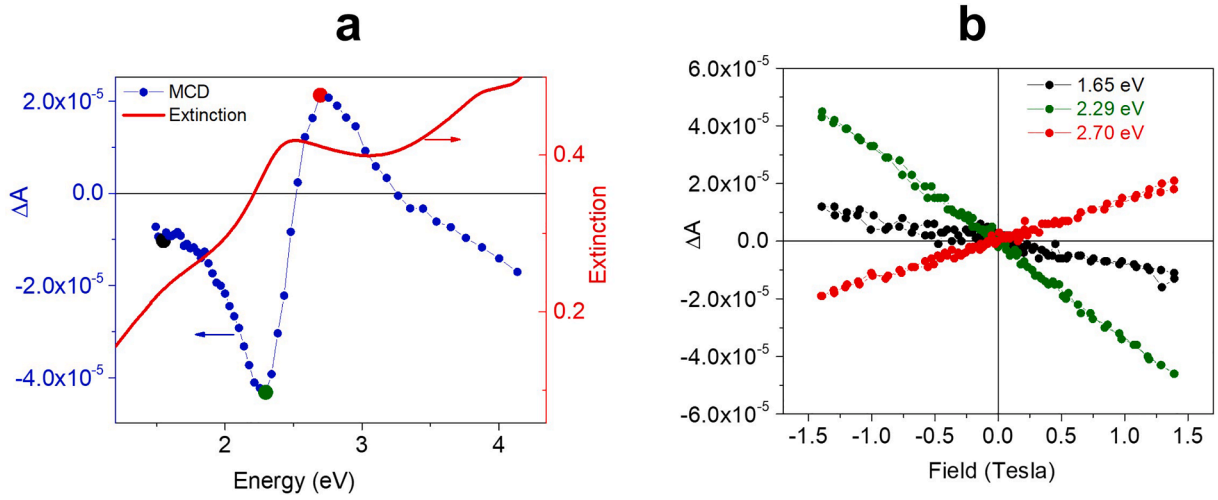

Fig. 9. a) UV–vis extinction spectrum and room temperature, and MCD spectrum at 1.4 Tesla for sample $Au_3Li_xFe_{1-x}$-264 °C dispersed in toluene; b) magnetic field dependence of the MCD signal collected at different photon energies, indicated in (a) with a dot of the corresponding color.

Au_3Li nanoalloys are easily synthesized by reacting Au seeds with BuLi, which acts as source of lithium. A plasmonic resonance around 500 nm is observed for $Au_3Li_xM_{1-x}$ nanoalloys, blue shifted with respect to pure Au NPs. The possibility to incorporate 3d magnetic metals suggests interesting applications in catalysis or photo-catalysis exploiting the plasmonic resonance to thermally activate chemical processes on the nanoalloy surface. Moreover, our findings open colloidal chemistry synthesis to unusual synthetic approaches that exploits Au, Au_3Li or Au_3MLi seeds as reactive templates for the synthesis of nanoparticle heterostructures or alloys.

4. Methods

Materials. $Fe(acac)_3$ (99%), $Ni(acac)_2$ and $HAuCl_4{\cdot}3H_2O$ were provided by Strem. Diphenyl ether (DPE) (99%), $Co(acac)_2$, (OLAM, 98%), Butyllithium (BuLi) (2.5 M in hexane), EtOH, and toluene were provided by Merck.

Synthesis of $Au_3Li_xM_{1-x}$ nanoalloys. All the synthetic steps were performed in an Ar atmosphere and under continuous magnetic stirring. In a 100 mL flask, 0.008 mmol of metal (Fe, Ni or Co) acetylacetonate and 0.025 mmol of $HAuCl_4{\cdot}3H_2O$ were dissolved in 10 mL of DPE with 1 mL of Oleylamine to prepare the metal precursor solution. In another flask, the reductant solution was prepared by adding 0.9 mL of BuLi solution (2.5 M in hexane) to 5 mL of DPE under Ar atmosphere. The hexane was removed from the flask under vacuum. The temperature of the precursor solution was increased up to 90 °C, and kept for 90 min, after which the reductant solution was added, and the temperature was raised to 250 °C during 80 min. The reaction mixture was then cooled to room temperature by removing the heating source, and the NPs were washed three times by centrifugation in EtOH (4400 g) and redispersion in toluene. Synthetic parameters were optimized as described in the results and discussion section.

X-ray Powder Diffraction. Powder X-ray Diffraction (XRPD) measurements were carried out using a Bruker D8 Advance diffractometer equipped with a Cu Kα radiation and operating in Theta-Theta Bragg Brentano geometry at 40 kV and 40 mA.

Inductively Coupled Plasma Atomic Emission Spectroscopy (ICP-AES). ICP-AES measurements were performed in triplicate by using a Varian 720-ES Inductively Coupled Plasma Atomic Emission Spectrometer, on samples (~3 mg) digested in concentrated aqua regia (HCl suprapure and HNO_3 sub-boiled in 3:1 ratio) and in the presence of H_2O_2, diluted with ultrapure water (≥18 MΩ/cm) and analyzed using

Ge as internal standard. Calibration standards were prepared by gravimetric serial dilution from monostandard at 1000 mg/L. According to previous studies performed with the same instrument, the standard deviation on the measurements can be considered below 10% for all the metal atoms used in this study.[58].

Transmission Electron Microscopy. Transmission Electron Microscopy (TEM) analysis was performed using a Philips CM12, operating at 100 kV. The samples were prepared by drop drying a dilute suspension of the nanoalloys in toluene onto 200 mesh carbon-coated copper grids. The mean size, standard deviation and size distribution were obtained from statistical analysis performed over at least 300 NPs.

Optical characterization. The UV–Vis absorption spectra were collected at room temperature with a V-670 (Jasco) spectrophotometer, using quartz cuvettes.

SQUID Magnetometry. Magnetic properties were investigated using a Quantum Design MPMS SQUID magnetometer on randomly oriented pressed powder pellets. The field was always applied parallel to the pellet plane. The magnetization was normalized for the total mass of the sample, and the diamagnetic contribution of the Teflon support was subtracted.

Magnetic Circular Dichroism. Magnetic Circular Dichroism (MCD) spectra were recorded at room temperature and with 1.4 Tesla of applied field on a dispersion of the nanoalloys in toluene, using a in-house built setup, which modulates the polarization of light between left-handed and right-handed using a photo-elastic modulator and takes advantage of phase sensitive detection with a lock-in amplifier. For further information on the magneto-optical setup see reference [43].

Declaration of Competing Interest

The authors declare that they have no known competing financial interests or personal relationships that could have appeared to influence the work reported in this paper.

Data availability

No data was used for the research described in the article.

Acknowledgements

A.G. and F.P. acknowledge the financial support of PRIN2017 under Grant No. 2017CR5WCH Q-ChiSS (Italian MIUR) and of PRA_2017_25 (Università di Pisa). Prof. Mirko Severi (University of Florence) is acknowledged for ICP-AES analysis.

Appendix A. Supplementary data

Picture of the aliquots taken during the synthesis of the nanoalloys. A representative TEM image and the XRPD diffractogram of Au seeds synthesized in situ in the first step of the synthetic route. A representative TEM image and the XRPD diffractogram of the nanoparticles obtained using a lithium-free reducing agent. Supplementary data to this article can be found online at https://doi.org/10.1016/j.ica.2023.121545.

References

[1] K.D. Gilroy, A. Ruditskiy, H.-C. Peng, D. Qin, Y. Xia, Bimetallic Nanocrystals: Syntheses, Properties, and Applications, Chem. Rev. 116 (2016) 10414–10472, https://doi.org/10.1021/acs.chemrev.6b00211.

[2] M.R. Buck, R.E. Schaak, Emerging Strategies for the Total Synthesis of Inorganic Nanostructures, Angew. Chem. Int. Ed. 52 (2013) 6154–6178, https://doi.org/10.1002/anie.201207240.

[3] C. Borri, M. Albino, C. Innocenti, F. Pineider, L. Cavigli, S. Centi, C. Sangregorio, F. Ratto, R. Pini, A bionic shuttle carrying multi-modular particles and holding tumor-tropic features, Mater. Sci. Eng.: C. 117 (2020), 111338, https://doi.org/10.1016/j.msec.2020.111338.

[4] B. Muzzi, M. Albino, M. Petrecca, C. Innocenti, C.d.J. Fernández, G. Bertoni, C. Marquina, M.R. Ibarra, C. Sangregorio, 3d Metal Doping of Core@Shell Wüstite@ferrite Nanoparticles as a Promising Route toward Room Temperature Exchange Bias Magnets, Small 18 (16) (2022) 2107426.

[5] B. Muzzi, M. Albino, A. Gabbani, A. Omelyanchik, E. Kozenkova, M. Petrecca, C. Innocenti, E. Balica, A. Lavacchi, F. Scavone, C. Anceschi, G. Petrucci, A. Ibarra, A. Laurenzana, F. Pineider, V. Rodionova, C. Sangregorio, Star-Shaped Magnetic-Plasmonic Au@Fe3O4 Nano-Heterostructures for Photothermal Therapy, ACS Appl. Mater. Interfaces 14 (2022) 29087–29098, https://doi.org/10.1021/acsami.2c04865.

[6] M.B. Cortie, A.M. McDonagh, Synthesis and Optical Properties of Hybrid and Alloy Plasmonic Nanoparticles, Chem. Rev. 111 (2011) 3713–3735, https://doi.org/10.1021/cr1002529.

[7] D. Wang, Y. Li, Bimetallic Nanocrystals: Liquid-Phase Synthesis and Catalytic Applications, Adv. Mater. 23 (2011) 1044–1060, https://doi.org/10.1002/adma.201003695.

[8] F. Varsano, M. Bellusci, A. La Barbera, M. Petrecca, M. Albino, C. Sangregorio, Dry reforming of methane powered by magnetic induction, Int. J. Hydrogen Energy 44 (2019) 21037–21044, https://doi.org/10.1016/j.ijhydene.2019.02.055.

[9] R. Ferrando, J. Jellinek, R.L. Johnston, Nanoalloys: From Theory to Applications of Alloy Clusters and Nanoparticles, Chem. Rev. 108 (2008) 845–910, https://doi.org/10.1021/cr040090g.

[10] M. Zhou, C. Li, J. Fang, Noble-Metal Based Random Alloy and Intermetallic Nanocrystals: Syntheses and Applications, Chem. Rev. 121 (2021) 736–795, https://doi.org/10.1021/acs.chemrev.0c00436.

[11] Y.a. Perlov, H. Ebert, A.N. Yaresko, V.N. Antonov, D. Weller, Influence of disorder on the magneto-optical properties of FePt, Solid State Commun. 105 (4) (1998) 273–278.

[12] S. Sun, Recent advances in chemical synthesis, self-assembly, and applications of FePt nanoparticles, Adv. Mater. 18 (4) (2006) 393–403.

[13] J.T.L. Gamler, H.M. Ashberry, S.E. Skrabalak, K.M. Koczkur, Random Alloyed versus Intermetallic Nanoparticles: A Comparison of Electrocatalytic Performance, Adv. Mater. 30 (2018) 1801563, https://doi.org/10.1002/adma.201801563.

[14] Y. Yan, J.S. Du, K.D. Gilroy, D. Yang, Y. Xia, H. Zhang, Intermetallic Nanocrystals: Syntheses and Catalytic Applications, Adv. Mater. 29 (2017) 1605997, https://doi.org/10.1002/adma.201605997.

[15] P. Pyykkö, Relativity, Gold, Closed-Shell Interactions, and CsAu· NH3, Angew. Chem. Int. Ed. 41 (2002) 3573–3578.

[16] J.D. Corbett, Exploratory Synthesis: The Fascinating and Diverse Chemistry of Polar Intermetallic Phases†This article is based on J. D. Corbett's address upon receipt of the 2008 American Chemical Society's F. Albert Cotton Award in Synthetic Inorganic Chemistry sponsored by the F. Albert Cotton Endowment Fund. Inorg. Chem. 49 (1) (2010) 13–28.

[17] P. Schwerdtfeger, M. Dolg, W.H.E. Schwarz, G.A. Bowmaker, P.D.W. Boyd, Relativistic effects in gold chemistry. I. Diatomic gold compounds, J. Chem. Phys. 91 (3) (1989) 1762–1774.

[18] R.E. Watson, M. Weinert, Charge transfer in gold–alkali-metal systems, Phys. Rev. B 49 (1994) 7148–7154, https://doi.org/10.1103/PhysRevB.49.7148.

[19] L. Agnarelli, Y. Prots, U. Burkhardt, M. Schmidt, P. Koželj, A. Leithe-Jasper, Y. Grin, Mg3Pt2: Anionic Chains in a Eu3Ga2-Type Structure, Inorg. Chem. 60 (2021) 13681–13690, https://doi.org/10.1021/acs.inorgchem.1c01995.

[20] R. Freccero, S.D. Negri, A. Saccone, P. Solokha, Solid state interactions in the La–Au–Mg system: phase equilibria, novel compounds and chemical bonding, Dalton Trans. 49 (2020) 12056–12067, https://doi.org/10.1039/D0DT02359K.

[21] P. Solokha, S. De Negri, V. Pavlyuk, A. Saccone, Anti-Mackay Polyicosahedral Clusters in La−Ni−Mg Ternary Compounds: Synthesis and Crystal Structure of the La43Ni17Mg5 New Intermetallic Phase, Inorg. Chem. 48 (2009) 11586–11593, https://doi.org/10.1021/ic901422v.

[22] L. Agnarelli, Y. Prots, M. Schmidt, M. Krnel, E. Svanidze, U. Burkhardt, A. Leithe-Jasper, Y. Grin, Be3Ru: Polar Multiatomic Bonding in the Closest Packing of Atoms, ChemistryOpen. 11 (2022) e202200118.

[23] T. Massalski, Binary alloy phase diagrams, American Society for Metals, 1986.

[24] V. Amendola, M. Meneghetti, O.M. Bakr, P. Riello, S. Polizzi, D.H. Anjum, S. Fiameni, P. Arosio, T. Orlando, C. de Julian Fernandez, F. Pineider, C. Sangregorio, A. Lascialfari, Coexistence of plasmonic and magnetic properties in Au89Fe11 nanoalloys, Nanoscale 5 (2013) 5611, https://doi.org/10.1039/c3nr01119d.

[25] V. Amendola, S. Scaramuzza, S. Agnoli, S. Polizzi, M. Meneghetti, Strong dependence of surface plasmon resonance and surface enhanced Raman scattering on the composition of Au–Fe nanoalloys, Nanoscale 6 (2014) 1423–1433, https://doi.org/10.1039/C3NR04995G.

[26] Y. Vasquez, Z. Luo, R.E. Schaak, Low-Temperature Solution Synthesis of the Non-Equilibrium Ordered Intermetallic Compounds Au $_3$ Fe, Au $_3$ Co, and Au $_3$ Ni as Nanocrystals, J. Am. Chem. Soc. 130 (2008) 11866–11867, https://doi.org/10.1021/ja804858u.

[27] S. Zhou, H. Yin, V. Schwartz, Z. Wu, D. Mullins, B. Eichhorn, S.H. Overbury, S. Dai, In Situ Phase Separation of NiAu Alloy Nanoparticles for Preparing Highly Active Au/NiO CO Oxidation Catalysts, ChemPhysChem 9 (2008) 2475–2479, https://doi.org/10.1002/cphc.200800587.

[28] J.F. Bondi, R. Misra, X. Ke, I.T. Sines, P. Schiffer, R.E. Schaak, Optimized Synthesis and Magnetic Properties of Intermetallic Au3Fe1−x, Au3Co1−x, and Au3Ni1−x Nanoparticles, Chem. Mater. 22 (2010) 3988–3994, https://doi.org/10.1021/cm100705c.

[29] J.F. Bondi, R.E. Schaak, Solution Chemistry Synthesis of Intermetallic Gold-Lithium Nanoparticles, Eur. J. Inorg. Chem. 2011 (2011) 3877–3880, https://doi.org/10.1002/ejic.201100276.

[30] V.K. LaMer, R.H. Dinegar, Theory, production and mechanism of formation of monodispersed hydrosols, J. Am. Chem. Soc. 72 (11) (1950) 4847–4854.
[31] S. Mourdikoudis, L.M. Liz-Marzán, Oleylamine in Nanoparticle Synthesis, Chem. Mater. 25 (2013) 1465–1476, https://doi.org/10.1021/cm4000476.
[32] H. Hiramatsu, F.E. Osterloh, A Simple Large-Scale Synthesis of Nearly Monodisperse Gold and Silver Nanoparticles with Adjustable Sizes and with Exchangeable Surfactants, Chem. Mater. 16 (2004) 2509–2511, https://doi.org/10.1021/cm049532v.
[33] H.M. Ashberry, J.T.L. Gamler, R.R. Unocic, S.E. Skrabalak, Disorder-to-Order Transition Mediated by Size Refocusing: A Route toward Monodisperse Intermetallic Nanoparticles, Nano Lett. 19 (2019) 6418–6423, https://doi.org/10.1021/acs.nanolett.9b02610.
[34] Y.K. Takahashi, T. Ohkubo, M. Ohnuma, K. Hono, Size effect on the ordering of FePt granular films, J. Appl. Phys. 93 (2003) 7166–7168, https://doi.org/10.1063/1.1555895.
[35] V. Amendola, R. Pilot, M. Frasconi, O.M. Maragò, M.A. Iatì, Surface plasmon resonance in gold nanoparticles: a review, J. Phys. Condens. Matter 29 (20) (2017) 203002.
[36] A. Agrawal, S.H. Cho, O. Zandi, S. Ghosh, R.W. Johns, D.J. Milliron, Localized Surface Plasmon Resonance in Semiconductor Nanocrystals, Chem. Rev. 118 (2018) 3121–3207, https://doi.org/10.1021/acs.chemrev.7b00613.
[37] Y. Zhang, S. He, W. Guo, Y. Hu, J. Huang, J.R. Mulcahy, W.D. Wei, Surface-Plasmon-Driven Hot Electron Photochemistry, Chem. Rev. 118 (6) (2018) 2927–2954.
[38] A. Mazzotta, A. Gabbani, M. Carlotti, M. Ruggeri, E. Fantechi, A. Ottomaniello, F. Pineider, A. Pucci, V. Mattoli, Invisible Thermoplasmonic Indium Tin Oxide Nanoparticle Ink for Anti-counterfeiting Applications, ACS Appl. Mater. Interfaces 14 (2022) 35276–35286, https://doi.org/10.1021/acsami.2c10864.
[39] E. Araya-Hermosilla, A. Gabbani, A. Mazzotta, M. Ruggeri, F. Orozco, V. Cappello, M. Gemmi, R.K. Bose, F. Picchioni, F. Pineider, V. Mattoli, A. Pucci, Rapid self-healing in IR-responsive plasmonic indium tin oxide/polyketone nanocomposites, J. Mater. Chem. A 10 (2022) 12957–12967, https://doi.org/10.1039/D2TA01286C.
[40] G. Baffou, R. Quidant, Thermo-plasmonics: using metallic nanostructures as nano-sources of heat, Laser Photonics Rev. 7 (2013) 171–187, https://doi.org/10.1002/lpor.201200003.
[41] J.N. Anker, W.P. Hall, O. Lyandres, N.C. Shah, J. Zhao, R.P. Van Duyne, Biosensing with plasmonic nanosensors, Nat. Mater. 7 (2008) 442–453, https://doi.org/10.1038/nmat2162.
[42] K.M. Mayer, J.H. Hafner, Localized Surface Plasmon Resonance Sensors, Chem. Rev. 111 (2011) 3828–3857, https://doi.org/10.1021/cr100313v.
[43] A. Gabbani, E. Fantechi, G. Petrucci, G. Campo, C. de Julián Fernández, P. Ghigna, L. Sorace, V. Bonanni, M. Gurioli, C. Sangregorio, F. Pineider, Dielectric Effects in FeOx-Coated Au Nanoparticles Boost the Magnetoplasmonic Response: Implications for Active Plasmonic Devices, ACS Appl, Nano Mater. 4 (2021) 1057–1066, https://doi.org/10.1021/acsanm.0c02588.
[44] M.G. Blaber, M.D. Arnold, M.J. Ford, Optical properties of intermetallic compounds from first principles calculations: a search for the ideal plasmonic material, J. Phys. Condens. Matter 21 (14) (2009) 144211.
[45] S.K. Ghosh, T. Pal, Interparticle Coupling Effect on the Surface Plasmon Resonance of Gold Nanoparticles: From Theory to Applications, Chem. Rev. 107 (2007) 4797–4862, https://doi.org/10.1021/cr0680282.
[46] A. Gabbani, G. Petrucci, F. Pineider, Magneto-optical methods for magnetoplasmonics in noble metal nanostructures, J. Appl. Phys. 129 (21) (2021) 211101.
[47] F. Pineider, G. Campo, V. Bonanni, C. de Julián Fernández, G. Mattei, A. Caneschi, D. Gatteschi, C. Sangregorio, Circular Magnetoplasmonic Modes in Gold Nanoparticles, Nano Lett. 13 (2013) 4785–4789, https://doi.org/10.1021/nl402394p.
[48] A. Gabbani, C. Sangregorio, B. Tandon, A. Nag, M. Gurioli, F. Pineider, Magnetoplasmonics beyond Metals: Ultrahigh Sensing Performance in Transparent Conductive Oxide Nanocrystals, Nano Lett. 22 (2022) 9036–9044, https://doi.org/10.1021/acs.nanolett.2c03383.
[49] N. Maccaferri, A. Berger, S. Bonetti, V. Bonanni, M. Kataja, Q.H. Qin, S. van Dijken, Z. Pirzadeh, A. Dmitriev, J. Nogués, J. Åkerman, P. Vavassori, Tuning the Magneto-Optical Response of Nanosize Ferromagnetic Ni Disks Using the Phase of Localized Plasmons, Phys. Rev. Lett. 111 (2013), 167401, https://doi.org/10.1103/PhysRevLett.111.167401.
[50] J. Kuttruff, A. Gabbani, G. Petrucci, Y. Zhao, M. Iarossi, E. Pedrueza-Villalmanzo, A. Dmitriev, A. Parracino, G. Strangi, F. De Angelis, D. Brida, F. Pineider, N. Maccaferri, Magneto-Optical Activity in Nonmagnetic Hyperbolic Nanoparticles, Phys. Rev. Lett. 127 (2021), 217402, https://doi.org/10.1103/PhysRevLett.127.217402.
[51] A. López-Ortega, M. Zapata-Herrera, N. Maccaferri, M. Pancaldi, M. Garcia, A. Chuvilin, P. Vavassori, Enhanced magnetic modulation of light polarization exploiting hybridization with multipolar dark plasmons in magnetoplasmonic nanocavities, Light Sci. Appl. 9 (2020) 1–14, https://doi.org/10.1038/s41377-020-0285-0.
[52] N. Maccaferri, A. Gabbani, F. Pineider, T. Kaihara, T. Tapani, P. Vavassori, Magnetoplasmonics in confined geometries: Current challenges and future opportunities, Appl. Phys. Lett. 122 (12) (2023) 120502.
[53] A. Gabbani, G. Campo, V. Bonanni, P. van Rhee, G. Bottaro, C. de Julián Fernández, V. Bello, E. Fantechi, F. Biccari, M. Gurioli, L. Armelao, C. Sangregorio, G. Mattei, P. Christianen, F. Pineider, High Magnetic Field Magneto-optics on Plasmonic Silica-Embedded Silver Nanoparticles, J. Phys. Chem. C 126 (2022) 1939–1945, https://doi.org/10.1021/acs.jpcc.1c09900.
[54] G. Petrucci, A. Gabbani, I. Faniayeu, E. Pedrueza-Villalmanzo, G. Cucinotta, M. Atzori, A. Dmitriev, F. Pineider, Macroscopic magneto-chiroptical metasurfaces, Appl. Phys. Lett. 118 (25) (2021) 251108.
[55] G. Armelles, B. Caballero, A. Cebollada, A. Garcia-Martin, D. Meneses-Rodríguez, Magnetic field modification of optical magnetic dipoles, Nano Lett. 15 (3) (2015) 2045–2049.
[56] A. López-Ortega, M. Takahashi, S. Maenosono, P. Vavassori, Plasmon Induced Magneto-Optical Enhancement in Metallic Ag/FeCo Core/Shell Nanoparticles Synthesized by Colloidal Chemistry, Nanoscale 10 (39) (2018) 18672–18679.
[57] P.K. Jain, Y. Xiao, R. Walsworth, A.E. Cohen, Surface Plasmon Resonance Enhanced Magneto-Optics (SuPREMO): Faraday Rotation Enhancement in Gold-Coated Iron Oxide Nanocrystals, Nano Lett. 9 (2009) 1644–1650, https://doi.org/10.1021/nl900007k.
[58] F. Rugi, R. Udisti, S. Becagli, D. Frosini, G. Giorgetti, G. Kuhn, M. Marconi, D. Monien, S. Nava, M. Severi, F. Talarico, R. Traversi, One-million year Rare Earth Element stratigraphies along an Antarctic marine sediment core, Microchem. J. 122 (2015) 164–171, https://doi.org/10.1016/j.microc.2015.04.020.